ELSEVIER

Journal of Nuclear Materials 281 (2000) 146–162

journal of nuclear materials

www.elsevier.nl/locate/jnucmat

Lattice parameter changes associated with the rim-structure formation in high burn-up UO_2 fuels by micro X-ray diffraction

J. Spino *, D. Papaioannou

European Commission, Joint Research Centre, Institute for Transuranium Elements, P.O. Box. 2340, D-76125 Karlsruhe, Germany

Received 13 April 2000; accepted 30 June 2000

Abstract

Radial variations of the lattice parameter and peak width of two high burn-up UO_2-fuels (67 and 80 GWd/tM) were measured by a specially developed micro-X-ray diffraction technique, allowing spectra acquisition with 30 μm spatial resolution. The results showed a significant but constant peak broadening, and a lattice parameter that increased towards the pellet edge and decreased again within the rim-zone. This lattice contraction coincided with other property changes in the rim region, i.e., porosity increase, hardness decrease and Xe depletion. In terms of local burn-ups, the lattice contraction followed the rate of the matrix Xe depletion measured by EMPA, exceeding greatly the contraction rate due to dissolved fission products. The observed behaviour can be equally explained by a saturation of single interstitials with subsequent recombination with excess vacancies, as by the saturation and enlargement of dislocation loops. The concentration and sizes of defects involved and their possible relation to the rim structure formation are discussed.

1. Introduction

The distortion of the UO_2 crystal lattice caused by neutron irradiation has been characterised in detail in the very low burn-up range between 10^{-6} and 1 GWd/tM [1–3] and with some depth in the range between 6 and 100 GWd/tM [4–8]. In the very low burn-up range, it has been shown that the neutron damage, manifested as a lattice expansion and a Bragg-peak broadening, reached a maximum at burn-ups around 0.01 GWd/tM and was almost completely recovered after the irradiation has reached about 1 GWd/tM [1–3]. For burn-ups close to the end of the first cycle in LWR's and above (>6 GWd/tM), renewed increase of the lattice expansion and peak-broadening had been found [4–9] with a trend to a saturation around and above 80 GWd/tM [4,6]. Also, X-ray diffraction studies with moderate beam collimation (500 μm-beam aperture) [5] confirmed that at relatively low exposures (18 GWd/tM) the damage increased towards $r/r_0 = 1$. Just at these average burn-ups (≅20 GWd/tM), the burn-up increase in the outer zone of PWR-fuels starts to become evident.

The accumulated lattice damage has been assigned as the main reason for the changes appearing in the rim zone at higher burn-ups [5–9]. TEM examinations have shown that with increasing burn-up, the damage is manifested primarily by an increase of the dislocation density [6–9], steadily growing up to ≃40 GWd/tM and apparently saturating at ≃80 GWd/tM [8]. Furthermore, it has been suggested [7–10] and also incorporated to models [11,12] that after progressive tangling of dislocations, a dislocation cell-structure is formed, giving rise to the grain subdivision typical of the rim material. However, the lattice expansion measured [5–8] cannot be straightforward assigned to dislocations. In principle, such an effect can be caused only by interstitial dislocation loops [13,14] which, on the other hand, have been described as the predominant type of dislocation at low burn-ups [20] and have been also found to exist at high burn-ups [8,10,18].

* Corresponding author. Tel.: +49-7247 951 233; fax: +49-7247 951 590.

E-mail address: jose.spino@itu.fzk.de (J. Spino).

0022-3115/00/$ - see front matter
PII: S0022-3115(00)00236-1

A possible masking effect of the lattice expansion results in PWR-fuels [5–8] is also the α-damage that occurs during cooling of the fuels, i.e., in the period between the discharge and the post-irradiation examinations. As determined in [19,20], this damage can be much higher than that caused by neutrons [1–3], due to the much lower defect recombination in the first case [21]. It is to be noted that like the expected fission damage, the α-damage would also increase towards the pellet edge with the burn-up profile, since this is also the trend followed by the generated α-emitting elements (Pu, Am, Cm). However, although expected to be high, especially at high burn-ups, the contribution of the α-damage in the measured lattice constants increase was estimated in [6] to be at most 20%.

To clarify some of these aspects but especially to investigate in detail possible dimensional changes during the rim structure formation, it was considered important to perform XRD studies of the fuels at the smallest possible radial intervals; e.g. at 50 μm steps. Previous studies of the microstructure and mechanical properties [22], and also Xe depletion studies of Walker [23], hereafter compared, were done at similar small radial intervals. For that purpose, an appropriate micro-beam device had to be developed [24], to focus the X-ray beam in regions not wider than 30 μm along the radius of a fuel pellet, allowing the acquisition of non-overlapping diffraction spectra at the intervals mentioned. Results of its application in two high-burn-up fuels are presented and discussed in this paper.

2. Experimental

2.1. Fuel samples

Two standard PWR fuel samples with 67 and 80 GWd/tM average burn-ups were analysed. Irradiation data and microstructure characterisation of the sample with 67 GWd/tM can be found in [22], as well as in [23] for the matrix Xe-profile determination. A similar set of data for the sample with 80 GWd/tM can be found in [25].

2.2. Micro XRD system, sample preparation and measuring procedure

Samples were examined in a shielded (θ–θ) X-ray diffractometer (Seifert X-3000) with a Bragg–Brentano configuration, equipped with a standard Cu-tube (normal-line focus) and a double collimated scintillation-counter detector (i.e., with anti-scatter and receiving slits). The accelerating voltage applied to the Cu-anode was 40 kV; the thereof estimated penetration depth of the examinations was in the range of 30 μm. To ensure the correct alignment of the sample with respect to the incident beam, the apparatus was additionally provided with a micro-(x,y,ϕ) sample-positioning table. Precise displacements of the sample at 5 μm steps for translations and fractions of degree steps for rotations were then possible. A development was also undertaken to provide the equipment with a beam concentrator with nominal aperture of $\simeq$15 μm, that was not commercially available. Through this beam concentrator, whose effective (projected) width on the sample surface was $\simeq$30 μm (see Section 2.3), an intensity win of about 100 times relative to a simple slit was obtained.

To maximise both, the diffracted intensity and the statistics of diffracting planes (grains) at a given radial position, the combination of longitudinal fuel sections and line-focused beam was adopted. The utilised configuration is illustrated in Fig. 1 for the sample with 80 GWd/tM, with beam dimensions: 3000 μm (length)$\times$ $\cong$30 μm (width) (the real dependence of the beam width on the incident angle is given in Section 2.3). The thickness of the embedded fuel-sample after successive cutting and grinding-polishing operations was $\leqslant$0.1 mm. Inclusion of markers in the sample holder and careful control of the sample width during preparation ensured that the exposed pellet surface corresponded to the longitudinal-diametric plane. In Fig. 1 also the starting misalignment angle (ϕ_m) between the pellet radius and the scanning direction (perpendicular to the beam axis) is shown. This angle had to be brought to 0 for the measurements, to get the incident beam cross-section parallel to the Zry–UO_2 interface. For that, an alignment-routine was followed, minimising the Zry–UO_2 interface-width, according to the procedure described in Section 2.3.

Measurements were carried out in the step-scanning mode. The angular increment was 0.005° and the counting time per interval 40–60 s. A Ni-filter was utilised to eliminate the incident Cu-K_β radiation, but no crystal monochromator was used to eliminate the Cu K_{α_2} line because of the intensity loss. The corresponding K_{α_1} and K_{α_2} lines for each Bragg-reflection were then resolved by an appropriate peak fitting routine [26]. For lattice parameter calculations, the resolved K_{α_1}-line was used. For elimination of the systematic errors, the extrapolation function a_{hkl} vs $\cos\theta_{hkl}/\tan\theta_{hkl}$ towards $\theta = 90°$ was employed [27]. Apart from that, important sources of error as goniometer zero shift and eccentricity of the incident beam with respect to the goniometer axis, were eliminated by careful system alignment. The whole procedure was checked by examination of Si, Au and UO_2 reference samples, whose lattice parameters were reproduced within an error band of $\pm$0.01 pm with respect to the tabulated values [28,29].

2.3. Microbeam resolution

The nominal aperture given to the beam concentrator was 15 μm; its real value and the effective beam width

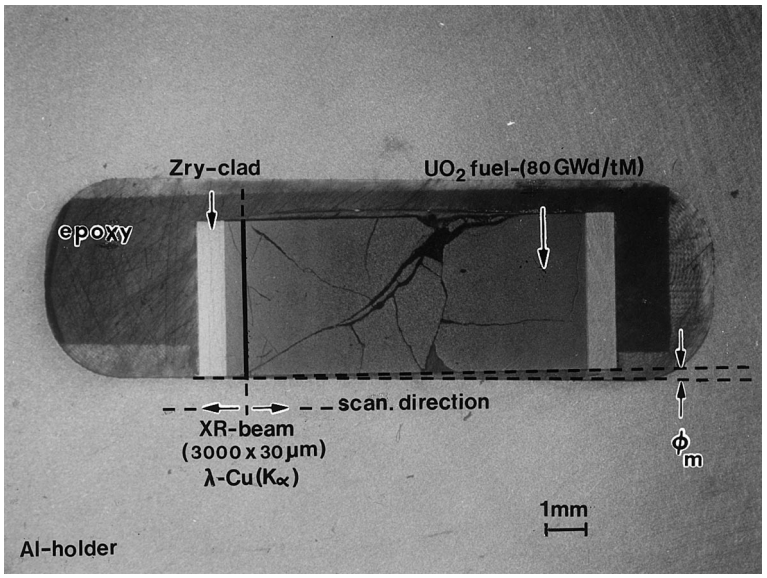

Fig. 1. PWR-fuel sample (80 GWd/tM) prepared for micro-XRD examinations. Sample thickness: ≅100 μm.

projected on the sample surface were determined experimentally. The employed procedure and results are shown in Fig. 2. This routine was based on the determination of a steel/CaF_2-crystal interface width, according to the extinction of the diffracted CaF_2 peaks while the sample was moved with respect to the incident beam. The displacements (in μm) needed for the extinction of the different peaks are plotted in Fig. 2 as function of the diffraction angle. It is to be noted that since the main CaF_2-crystal plane did not coincide exactly with the prepared surface, the measured diffraction angles differed slightly from the tabulated Bragg angles.

Considering the analytical expression for the beam width projection ($y(\theta) = \text{aperture}/\sin\theta$), fitting of the results in Fig. 2 indicates a nominal beam aperture of 13–15 μm and a projected beam width of 30 μm or less for $\theta > 25°$. Taking into account the angular position of the UO_2 peaks (marked in Fig. 2), it was confirmed that diffraction spectra of the fuels obtained at radial intervals of 50 μm showed essentially no overlapping (Fig. 2).

2.4. Porosity and micro-hardness determinations

As a complement of the XRD analysis, the evolution of the affected rim-zone of the two samples studied had been assessed by porosity and micro-hardness measurements. The porosity was determined by image analysis, by the same method described in [22], though in the present case more enlarged micrographs (magnification: 1600 X) were used. For the Vickers-indentation tests also the same procedure as described in [22] was used, utilising a load of 0.5N (such measurements are designated as $HV_{0.5N}$).

2.5. Simulated fuels

To separate the effect of the irradiation damage from those lattice dimension changes caused by chemical effects (i.e., fission products, actinides and oxygen incorporations into the fcc-matrix lattice), the variation of the UO_2 lattice constant with the concentration of dissolved metal atoms (burn-up) and the oxygen-to-metal ratio (O/M) is needed. Nevertheless, since the fuel under irradiation remains essentially stoichiometric (see details in Section 4.1), mainly the effect of the fission products and actinides incorporations (at O/M = 2) is important. This is best obtained from the annealed (defect free) fuel samples under neutral or light reducing atmospheres [4–6], but these data are not fully available for the whole local burn-up range analysed here. As a good complement, simulated fuel samples can be used, for which we include here a revised set of own simulated fuels data partially published in [30], extending the existing literature data from about 80 GWd/tM [31–34] to approximately 220 GWd/tM.

Preparation details of these simulated fuels including most of the fission products and actinides (simulated) with compositions equal to the real fuel according to ORIGEN-2 [35] calculations have been described elsewhere [30]. Here, it is remarked that the U content checked by coulometric titration indicated a simulated burn-up uncertainty of ±3%, while the minor elements analysis, done by EMPA and ICP-MS, gave a burn-up uncertainty of less than ±8%, compared to the calculated values (ORIGEN-2). With respect to the oxygen stoichiometry, it was assumed that the sintering of the samples under an $Ar + 5\%H_2$ atmosphere assured an

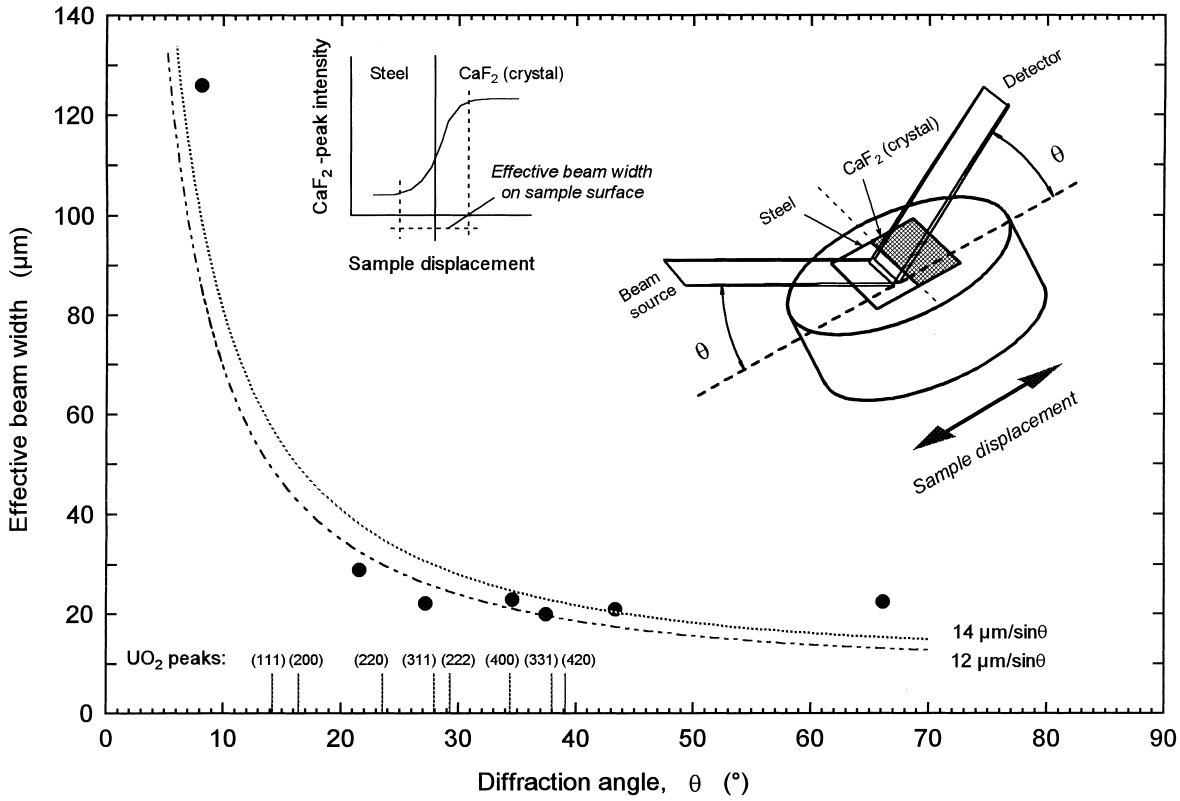

Fig. 2. Micro-beam resolution test on a CaF_2/steel interface. Nominal beam aperture = 15 μm. Dotted fitting curves: $y(\theta)$ = beam aperture/sin θ (theoretical angular dependence of projected beam).

O/M ratio close to 2. Remarkable was also a detected excess of ZrO_2 and Y_2O_3 below ≅100 GWd/tM, arising from a contamination during the milling step of the fabrication process (mill container and balls done of these materials). This decreased in part additionally the lattice constants at the lower simulated burn-ups, although not above ≃100 GWd/tM where the ZrO_2/Y_2O_3-contamination was insignificant with respect to the total amount of added foreign elements (see Section 4.1).

3. Results

3.1. Lattice distortion across the irradiated fuel radius

Fig. 3 shows an example of the lattice distortion (i.e., peak shift, intensity loss and line broadening) caused by irradiation (plus α-in-growth) damage, as recorded for the (1 1 1)-peak of the fuel with 80 GWd/tM (radial position $r/r_0 = 0.745$). In that case, as compared to the (1 1 1)-reflection of unirradiated UO_2 under the same conditions, the peak shift was of about −0.02° ($\Delta\theta < 0$, dilatation), the intensity loss about 10 times and the increase of the full width at half-maximum intensity (FWHM) about 200% (Fig. 3). It is also noted that the otherwise good resolution of the equipment for the K_{α_1}–K_{α_2} doublet even at low diffraction angles (≃14°) (Fig. 3), was sensibly decreased owing to the lattice distortion. Due to this distortion, also the ($h\,k\,l$)-peaks above (4 2 0) became not measurable, which reduced the accuracy of the lattice parameter determinations (extrapolation to $\theta = 90°$), usually improved by the higher ($h\,k\,l$)-reflections.

Fig. 4 shows a synthesis of the results obtained for the two fuels examined, in terms of the Bragg-peak shift ($\Delta\theta_{h\,k\,l}$) and the line broadening ($\Delta\mathrm{FWHM}_{h\,k\,l}/\mathrm{FWHM}_{h\,k\,l}$) across the pellet radius. The Bragg-peak broadening values for single ($h\,k\,l$)-reflections appeared more or less constant over the pellet radius for both fuels (Figs. 4(a) and (b), upper curves). Contrarily, the individual peak shifts ($\Delta\theta_{h\,k\,l} < 0$, lattice dilatations) showed a maximum around $r/r_0 = 0.9$ for the sample with 67 GWd/tM, and around $r/r_0 = 0.75$–0.8 for the sample with 80 GWd/tM (Figs. 4(a) and (b), lower curves). The enhancement of the peak-shift profiles for higher ($h\,k\,l$)-reflections obeyed in principle to the proportionality $\Delta\theta_{h\,k\,l} \propto \tan\theta_{h\,k\,l}$ [16]. For both fuels, the pellet radius could be then divided in three zones of increasing (I),

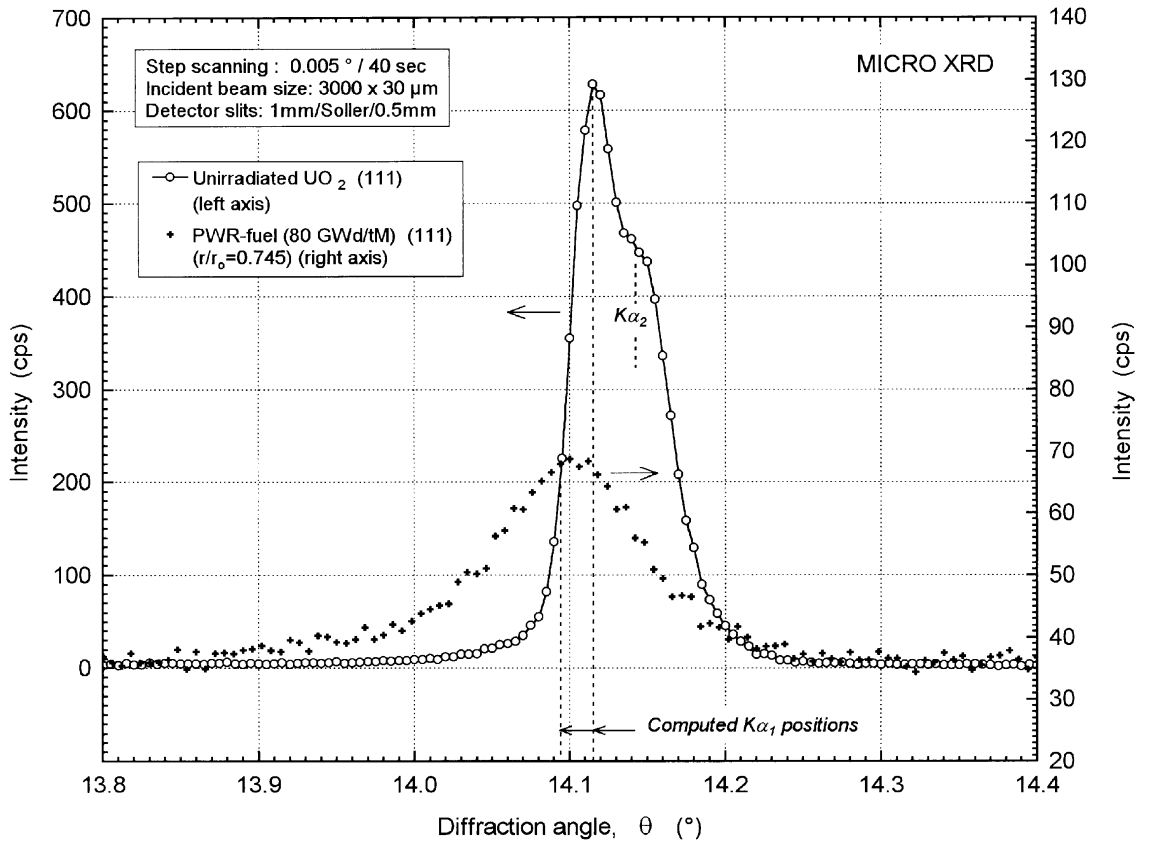

Fig. 3. Example of the (1 1 1)-reflection of the 80 GWd/tM-fuel at $r/r_0 = 0.505$ showing the magnitude of intensity loss, peak-shift and peak-broadening caused by radiation damage, as compared to unirradiated UO_2 under the same experimental conditions.

maximum (II) and decreasing (III) lattice dilatation, i.e., at the central, intermediate and outer radial positions (Fig. 4). As confirmed by the variation of other properties, the outer extreme of zone II coincided approximately with the onset of the rim-zone in both fuels (see next section). Remarkably, the width of this zone II (transition zone) was much larger for the fuel with 80 GWd/tM.

3.2. Lattice parameter variation

As mentioned in the experiments description, the lattice parameter at a given radial position was determined by extrapolation of the plot $a_{h\,k\,l}$ vs $\cos\theta_{h\,k\,l}/\tan\theta_{h\,k\,l}$ towards $\theta = 90°$ [27]. The accuracy of the extrapolated values at $\theta = 90°$ is governed essentially by the scatter of the individual $a_{h\,k\,l}$-results around the average slope determined by linear regression. As this denotes also the degree of damage in the lattice, a larger scatter of the individual results was corroborated for the irradiated fuels as for unirradiated UO_2. Thus, taking the most unfavourable case for the irradiated fuels this inaccuracy was ±0.09 pm ($\Delta a/a \simeq \pm 0.02\%$), while for unirradiated UO_2 this was only ±0.02 pm ($\Delta a/a \simeq \pm 0.004\%$).

The obtained lattice parameter results are plotted as function of the fuel radius in Figs. 5(a) and (b) for the fuels with 67 and 80 GWd/tM burn-up. In the figures also the corresponding microhardness ($HV_{0.5N}$) and porosity results are plotted, as well as the local burn-up profiles obtained by calculations with the APOLLO-2 code [36]. The scatter band of the lattice parameter values in Fig. 5 corresponds to the largest inaccuracy obtained in the extrapolations to $\theta = 90°$. In agreement with Fig. 4, it is shown that three different radial zones can also be established in terms of the lattice parameter, showing a maximum plateau of it at $r/r_0 \simeq 0.85$–0.92 for the fuel with 67 GWd/tM, and at $r/r_0 \simeq 0.62$–0.78 for the fuel with 80 GWd/tM burn-up.

The decrease of the lattice constant toward the pellet centre is attributed to thermal healing effects (Fig. 5). In contrast, the decrease towards the pellet edge is attributed to the formation of the rim structure, for which temperature effects are basically excluded. This is corroborated in principle by the radial profiles of the other properties plotted in Fig. 5, showing congruent

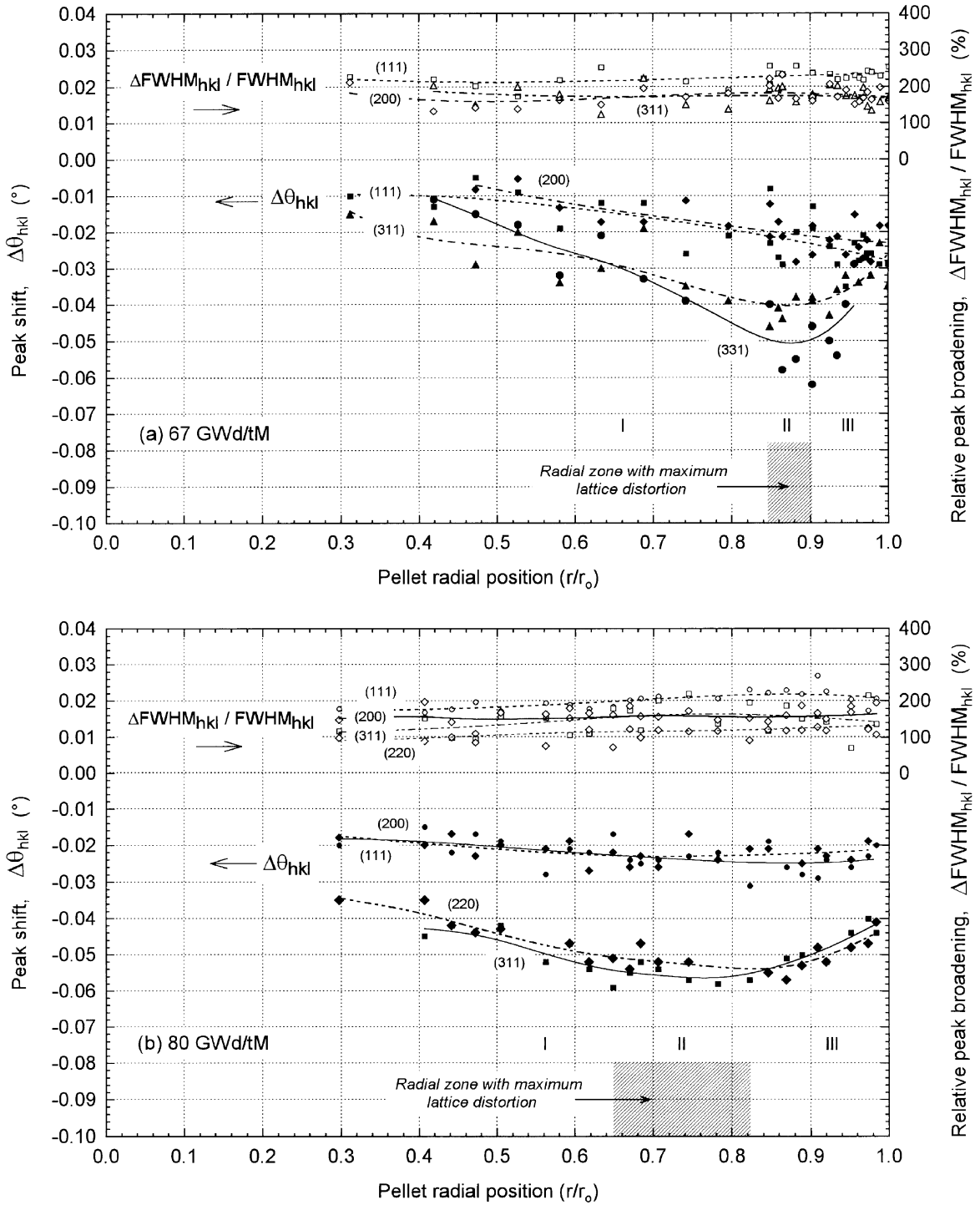

Fig. 4. Peak-broadening and peak-shift for various ($h\,k\,l$)-reflections across the pellet radius for the 67 and 80 GWd/tM-fuels (respectively, top and bottom figures), as determined by micro-XRD (30 μm-beam).

variations within the rim-zone. However, many parameters intervene in the configuration of such a profile, including the superimposed α- and fission damage, thermal healing effects, lattice dimension changes due to dissolution of fission products and actinides (Pu) and possibly oxygen in the UO_2-structure and finally the

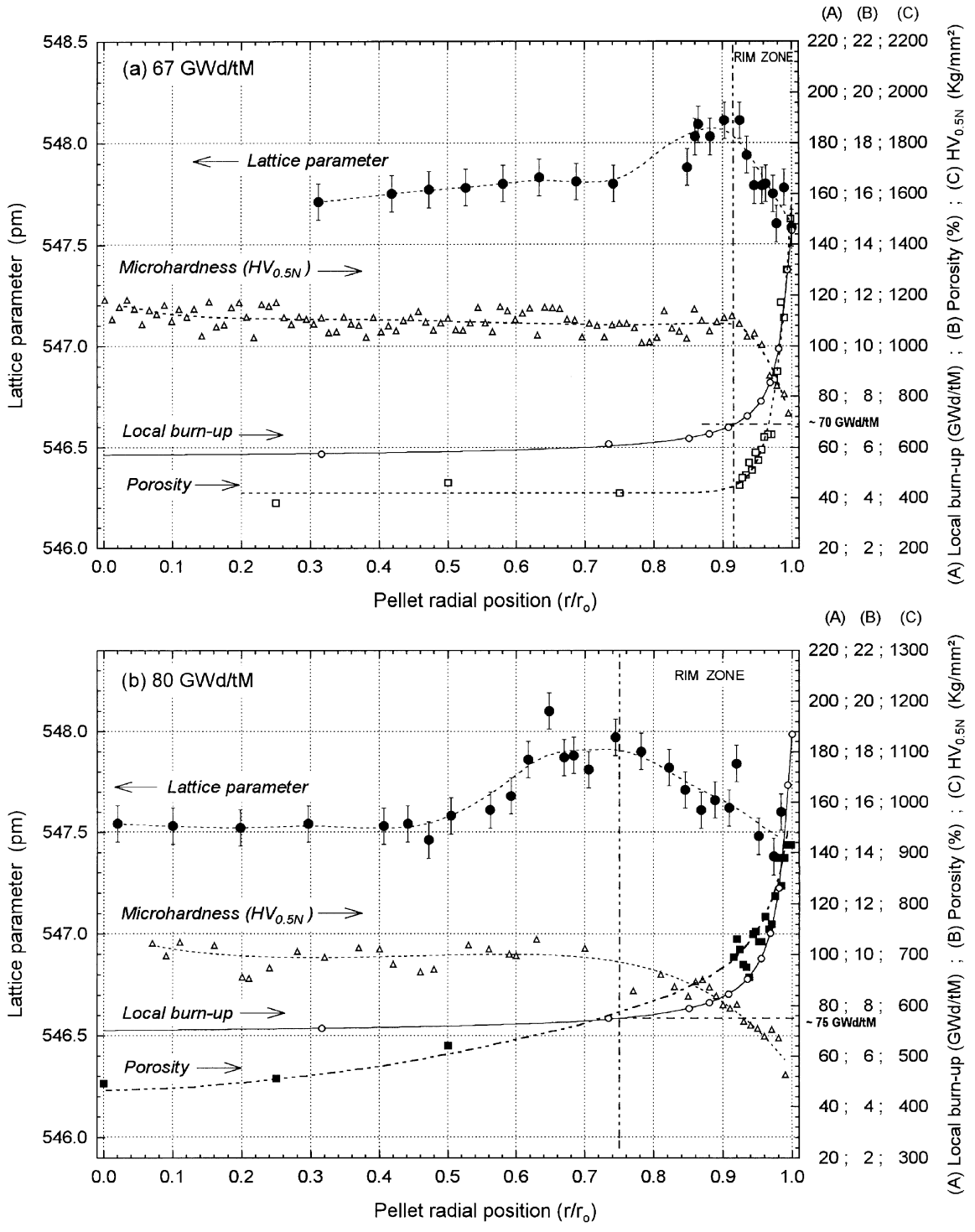

Fig. 5. Lattice parameters as a function of the radial position for the 67 GWd/tM and 80 GWd/tM fuels (respectively, top and bottom figures). Comparison with radial profiles of local burn-up (APOLLO-2 calculations), microhardness ($HV_{0.5N}$) and porosity (from quantitative metallography).

strict local burn-up effects associated with the rim-structure formation. In the following discussion, separate analysis of these multiple contributions is attempted.

4. Discussion

4.1. UO_2-lattice contraction due to chemical effects

Incorporations of oxygen, fission products and actinides into the fuel lattice produce in general a decrease of its lattice parameter. Here it is considered that the fuel remains in the stoichiometric condition (O/M = 2), assuming that the oxygen excess created during fission [37,38] is fully neutralised by the oxidation of Mo (in metallic precipitates) and of the inner Zr-cladding surface [39]. In fact, O/M measurements by the solid electrolyte technique confirmed the absence of fuel oxidation in both low [5] and high burn-up [40] fuels.

The effect of foreign atom dissolution in the UO_2 lattice is shown in Fig. 6 as function of burn-up. In Fig. 6, the available literature data up to ≃80 GWd/tM of irradiated and annealed fuels [4–6,41] and simulated fuels [31–34], as well as extended simulated fuel data produced in our laboratories (details in Section 2.5) [30] and elsewhere [42], are considered. Fig. 6 shows also Vegard's law calculations of the lattice parameter based on the fission atoms and actinides concentrations computed with the ORIGEN-2 code [35] and the single element contributions (lattice expansion/contraction) as reviewed by Kleykamp [43], assuming various percentages of dissolved Zr in UO_2. As pointed out in [43], sharing of Zr between the UO_2-lattice and the so-called 'grey-phase' precipitates (i.e., ABO_3 complexes with cubic perovskite-type structure, with Ba,Sr and Cs in A-sites and Zr,Mo,U,Pu and rear earths in B-sites) [38,44] largely controls the lattice dimension of the fuel, because of the large contraction effect of Zr.

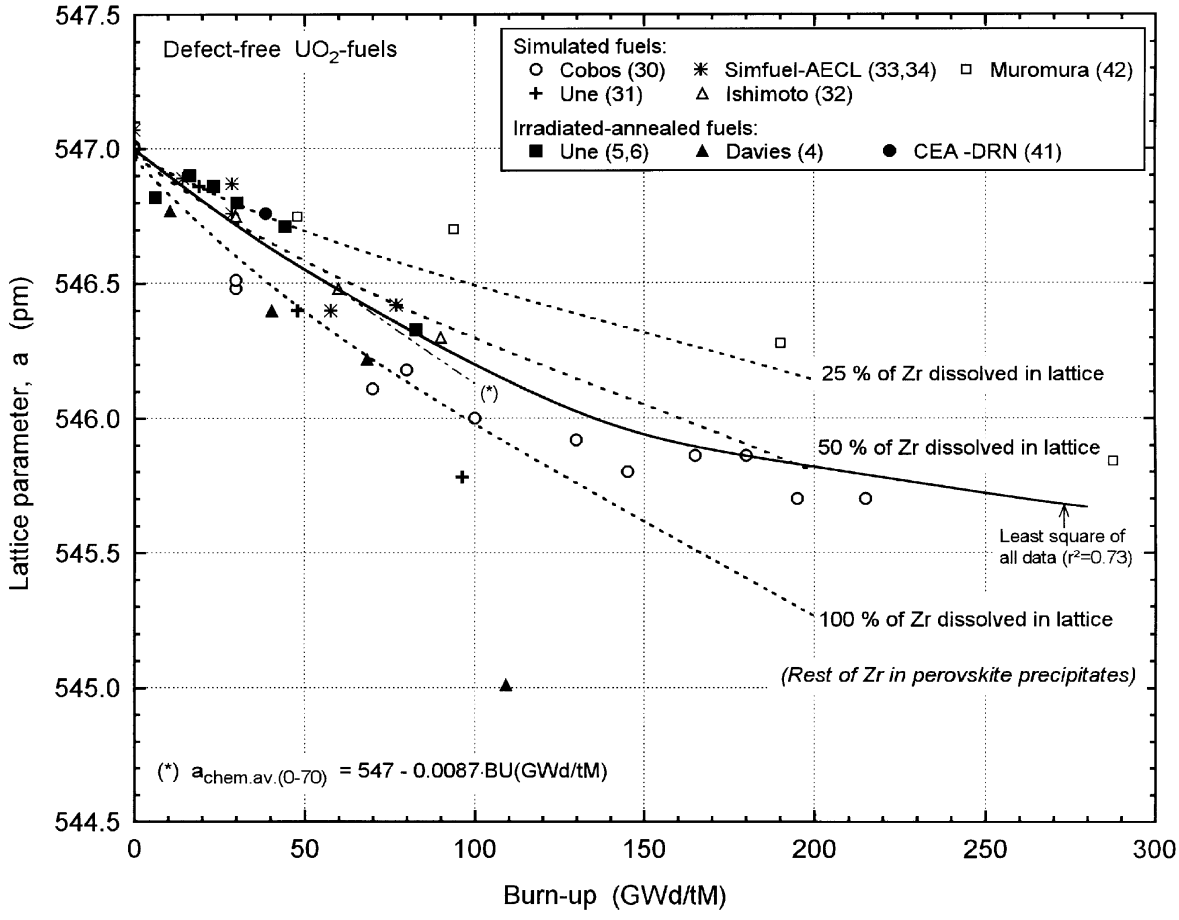

Fig. 6. Lattice parameter of simulated and annealed (defect free)-irradiated fuels as a function of burn-up. Dotted lines: Vegard's calculations with ORIGEN-2 compositions and single elements contributions according to Kleykamp [43], assuming 25%, 50% and 100% dissolution of Zr in the fuel lattice.

Though there is scatter in the experimental results, the average (best fit) of all data appears to coincide in general well with the assumption of 50% dissolution of Zr in the UO_2 lattice. However, based on composition analysis of the grey phase precipitates in irradiated fuels [38,44] and on phase equilibrium studies in the system $BaO–UO_2–ZrO_2–MoO_2$ [45], Kleykamp proposed a maximum of 25% dissolution of Zr in the fuel matrix, the rest being precipitated in the perovskite-phase [43]. This prediction was addressed, however, to LWR-fuels at low to moderate burn-ups and could eventually change at higher burn-ups. Further studies of the fuel precipitates composition in the burn-up range 80–200 GWd/tM appear therefore worthy. For our purpose in further analysis, an average lattice contraction rate of 0.087 pm/10 GWd/tM, corresponding to the best fit-slope in the range 0–70 GWd/tM, is assigned to the dissolution of foreign atoms. Similar contraction rates, i.e., 0.08–0.09 pm/10 GWd/tM, have been proposed in other analyses of irradiated LWR-fuels [39,43] and also for FBR-fuels [46]. For burn-ups above 100 GWd/tM, the assumed slope overestimates the results and constitutes a conservative limit of the (maximum) contraction rate of the fuel lattice due to chemical effects.

4.2. Lattice parameter of irradiated fuels vs Burn-up ($T < 800°C$)

It has been mentioned in Section 3.2 that several effects contribute to the form of the lattice parameter profiles shown in Figs. 5(a) and (b) and that, among others, the decrease of the values in the pellet centre may be due to thermal effects. This last can be also deduced from the XRD-results of Une et al. [5], where except for the here determined decrease of the values in the rim zone, similar lattice parameter profiles have been obtained at 18 and 35 GWd/tM, using a comparatively coarser beam collimation (500 μm). From Fig. 5 of [5], it is clear that the lattice parameter at $r/r_0 <\simeq 0.8$ was more decreased in the 35 GWd/tM fuel (power ramped) than in the 18 GWd/tM fuel (base irradiated). This indicates a priori an enhanced damage healing effect, due to temperature increase, in the centre of the power ramped fuel. In view of this, in the present analysis, only the transition and rim zones will be considered (i.e., $r/r_0 > 0.85$ for the 67 GWd/tM fuel and $r/r_0 > 0.62$ for the 80 GWd/tM fuel), excluding the more central regions where thermal effects could have influenced the results (Figs. 4 and 5).

The corresponding results of Fig. 5 for the outer radii are then plotted in Fig. 7 as function of the calculated local burn-up (APOLLO-2 code [36]), together with equivalent data of other authors [4–9,41]. For the case of Une et al. [5] also a burn-up correction for the rim zone was considered. It appears that data follow an exponential growth with burn-up up to about 70 GWd/tM, with a sharp decrease above this value (Fig. 7, upper curve). A similar cut-off has been also suggested by Une et al. [6] (see Fig. 3 in Ref. [6]), though at somewhat lower local burn-ups. This abrupt lattice contraction is a priori associated with the rim-structure formation. As suggested by the dotted slopes drawn in Fig. 7, the lattice contraction rate at the beginning of this transition (−0.8 pm/10 GWd/tM) exceeds in about 10 times the contraction rate due to dissolution of foreign atoms (−0.087 pm/10 GWd/tM, Section 4.1, Fig. 6). This may exclude solution effects as a triggering factor for the transformation.

It is noted that after the rather rapid transition at about 70–80 GWd/tM (Fig. 7), the lattice parameter tends again to a low constant level (region about 100–150 GWd/tM). These saturated values, corresponding to radial positions with maximum local burn-ups (also highest concentration of α-emitting elements), are here assumed to represent the maximum local α-damage. As a function of burn-up it is assumed that this damage would follow a similar saturating growth curve as the pure α-damage in UO_2 [19,20] (as the dotted saturating curve shown in Fig. 7). Although very approximate (not all fuels had the same enrichments and cooling times, both influencing the results), an assumption like this was necessary, since any attempt to suppress the α-damage by thermal annealing would also largely eliminate the fission-damage, impeding its characterization. As corroboration, Fig. 7 includes the annealed/aged data of Ref. [41]. It is shown that even after the largest aging-time recorded (3.4 yr) [41], the lattice constant increase after annealing did not surpass the assumed α-damage boundary. This limit, also exceeding the 20% α-damage contribution assumed in [6], is thus considered to be conservative.

4.3. The deduced fission-damage in the range 10–150 GWd/tM

Fig. 8 shows the relative lattice dimension change ($\Delta a/a_0$) after subtraction of the assumed α-damage in Fig. 7, taking the lattice constant of unirradiated UO_2 ($a_0 = 547$ pm) as reference. For reasons of comparison, the data without this subtraction are plotted in logarithmic burn-up scale in Fig. 9 together with the literature data at very low burn-ups [1–3]. As clearly seen in this figure, though important at high burn-ups, the assumed α-damage in the low burn-up range is negligible.

Similar to the cases of the low-dose fission-damage of UO_2 [1–3,47–49] and other ceramics [48–50], the data of Fig. 8 can be well described by first-order reaction rate equations. The basic assumption in this case is that the relative lattice volume change is proportional to the concentration of certain defects created or annihilated

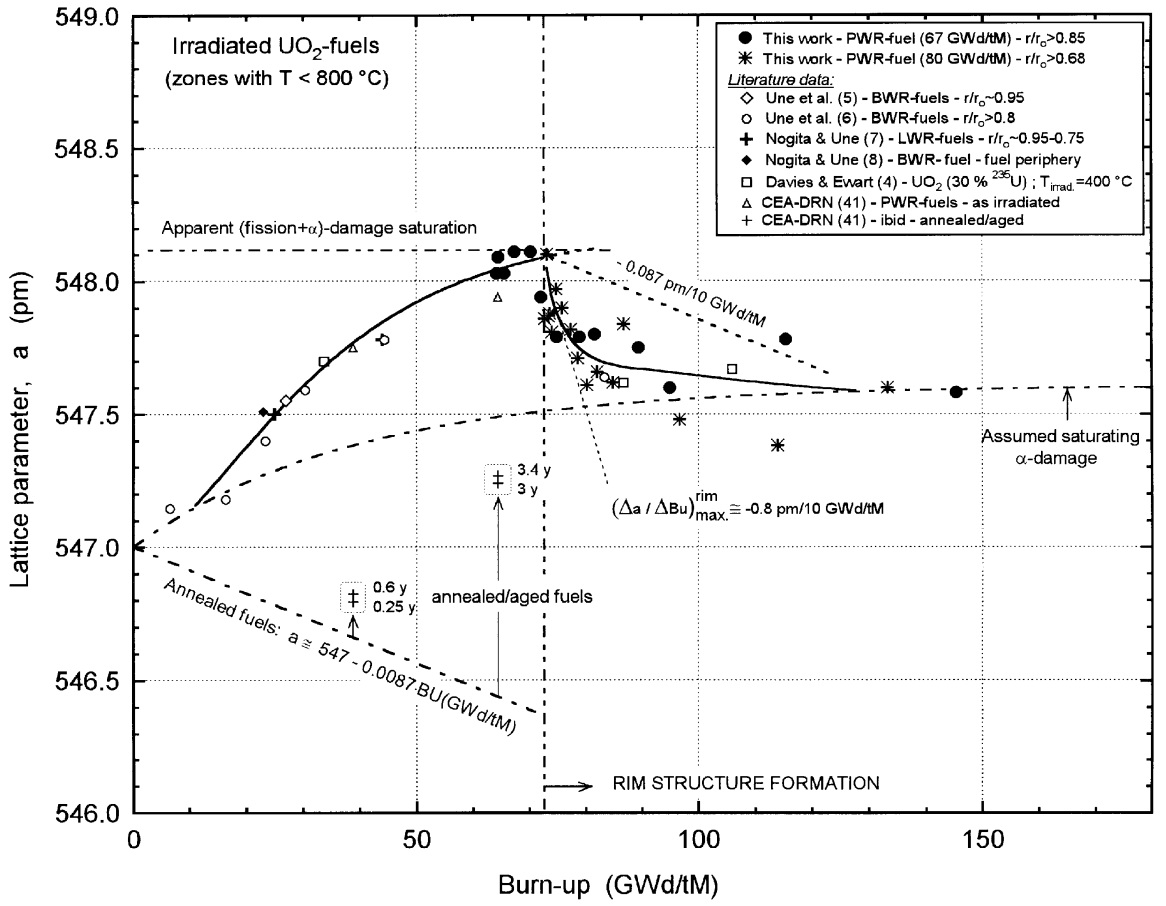

Fig. 7. Lattice parameter of the present irradiated fuels as function of the local burn-up, for radial regions near and after the maxima in Fig. 5. Comparison with literature data at lower burn-ups and with values of annealed/aged fuels (pure α-damage) [41]. Assumed saturating α-damage contribution: a_α (pm) $= 547 + 0.606[1 - \exp(-0.0257BU(\mathrm{GWd/tM}))]$. Annealed/aged fuels [41]: indicated aging time in years.

during fission, whose formation (or decay) rate obeys a first-order kinetic equation, i.e., $\mathrm{d}C/\mathrm{d}t = k(1 - C)$ for formation or $-\mathrm{d}C/\mathrm{d}t = kC$ for decay, with the variable time appearing as the quotient between burn-up (fission dose) and fission rate [3,47–50].

Since Frenkel defect pairs (1 interstitial + 1 vacancy) induce a net lattice expansion [19,47], authors of [3,47–49] attributed the lattice expansion phase in UO_2 at $\leqslant 0.01$ GWd/tM (Fig. 9, left) to the formation and saturation of these kinds of defects with burn-up. The subsequent lattice contraction phase was then assigned to the recombination with Schottky defects (vacancies + ad-atoms in boundaries), these last appearing in excess above $\simeq 0.01$ GWd/tM [3,47–49]. Applying here the same concepts and considering that a Frenkel pair in UO_2 causes a lattice volume increase of about one mean lattice atomic volume Ω ($\approx a^3/12$ with a = lattice constant) [47], the equations underlying the fitting functions in Fig. 8 became [3,47–50]

$$\Delta a/a_o = 1/3(N_{\mathrm{d1}}/V_{\mathrm{d1}})\Omega(1 - \exp(-V_{\mathrm{d1}}(BU - BU_1)))$$
(pre-transition, formation step) and
$$\Delta a/a_o = 1/3(N_{\mathrm{d2}}/V_{\mathrm{d2}})\Omega\exp(-V_{\mathrm{d2}}(BU - BU_2))$$
(post-transition, decay step) (1)

with N_{d1}, N_{d2} = numbers of defects remaining per fission, V_{d1}, V_{d2} = damaged volumes per fission and BU_1, BU_2 = characteristic burn-ups (or incubation times) at which each regime is established. It is remarked that data before transition in Fig. 8 (formation step) can be described either by a single reaction with incubation time (characteristic burn-up) or by a sequence of two first-order-reactions starting from time 0. The same was described in the case of neutron irradiation of ThO_2 at very low doses ($<10^{18}$ fissions/cm^3) [50], indicating the eventual formation of an intermediate defect before the predominant one was created.

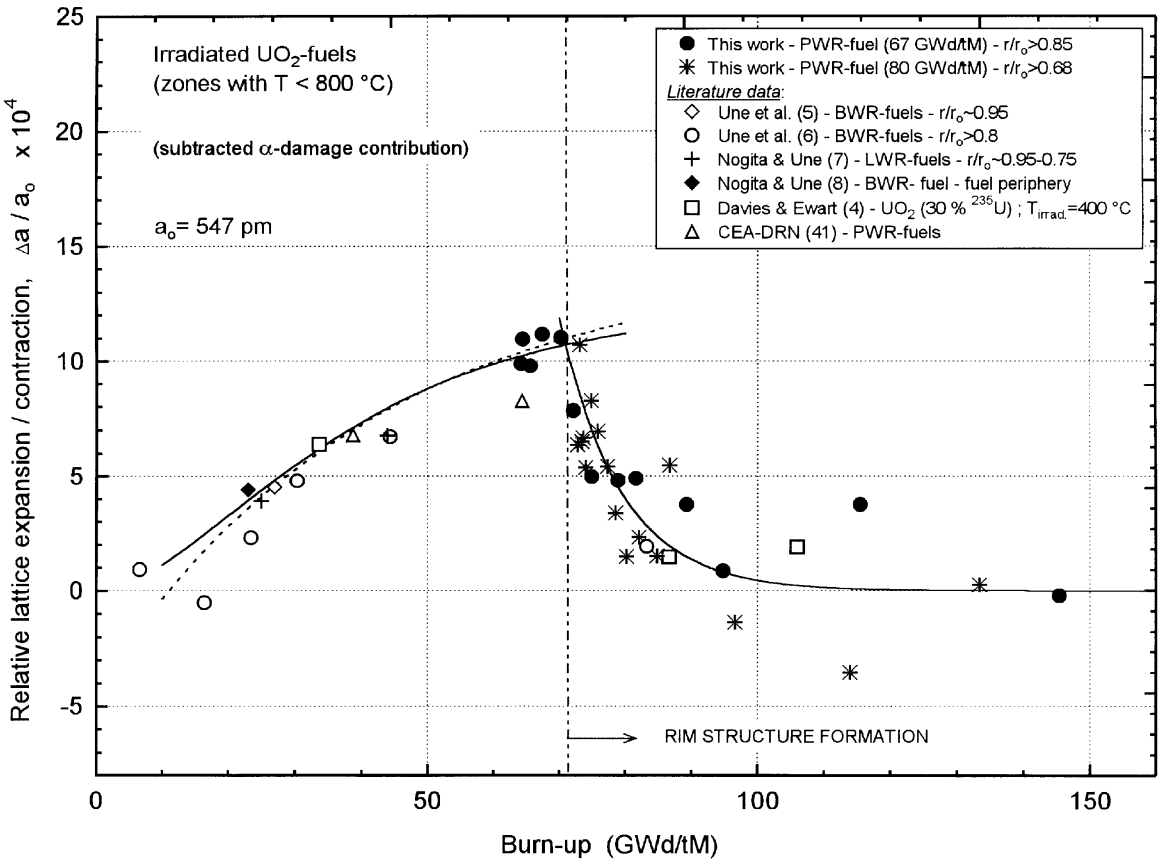

Fig. 8. Lattice expansion and contraction of irradiated fuels relative to unirradiated UO_2 as a function of the local burn-up. Same data as in Fig. 7 after subtraction of the assumed α-damage contribution. Fitting curves: pre-transition: (dotted line) $y = 14.44 \times 10^{-4}[1 - \exp(-0.024(BU - 11))]$ (1 step reaction); (full line) $y = 12.43 \times 10^{-4}\{1 + [0.060\exp(-0.042BU) - 0.042\exp(-0.060BU)]/(0.042 - 0.060)\}$ (2 steps reaction). Post-transition: $y = 11.88 \times 10^{-4}\exp(-0.108(BU - 70))$ (1 step reaction).

From the above equations and the fitting parameters in Fig. 8, the set of values $V_{d1} = 8.6 \times 10^{-22}$ cm^3/fission; $N_{d1} = 0.27$ fission^{-1} and $V_{d2} = 3.9 \times 10^{-22}$ cm^3/fission; $N_{d2} = 1.02$ fission^{-1} were derived for the transition around 70 GWd/tM. In contrast, for the damage peak at 0.01 GWd/tM (Fig. 9, left) values of $V_d \simeq 10^{-16}$–10^{-17} cm^3/fission and $N_d \simeq 1$–4×10^4 fission^{-1} were obtained [3,47–49]. This indicates similar defect concentrations per unit of damaged volume in the two burn-up ranges (N_d/V_d ratios), but $\simeq 10^4$ less surviving defects per fission at 70 GWd/tM than at 0.01 GWd/tM (N_d values). Considering that per fission event about 10^5 primary defects are produced [51], this implies a defect recombination ratio of 60–90% at 0.01 GWd/tM (Matzke indicates 80% for this range [51]), though ratios are >99.9999% at 70 GWd/tM. This extremely high defect recombination ratio at high exposures would suggest an underestimation of the remaining defects number, or alternatively a multiple association of primary defects in clusters.

4.4. Possible role of interstitial-dislocation loops

One possibility to contemplate defect association is to take into account the formation of interstitial dislocation loops. This kind of defect has been found to predominate in the low burn-up range [17] and has been also reported for high burn-up fuels in coexistence with tangled dislocations [8,10,18]. As proposed originally by Keating and Goland [13,14] and extensively treated in the book of Krivoglaz [16], when dislocation loops are large enough compared to the inter-atomic distances but small compared to the crystal dimensions, they produce a measurable lattice distortion that can be expressed as [16]

$$\Delta a/a = 1/3 N_L \Delta v^{loop}, \quad (2)$$

where N_L is the volumetric dislocation loop density and Δv^{loop} is the lattice volume change per loop $= \pi R_0^2 b$, where R_0 is the loop radius and b is the Burgers vector

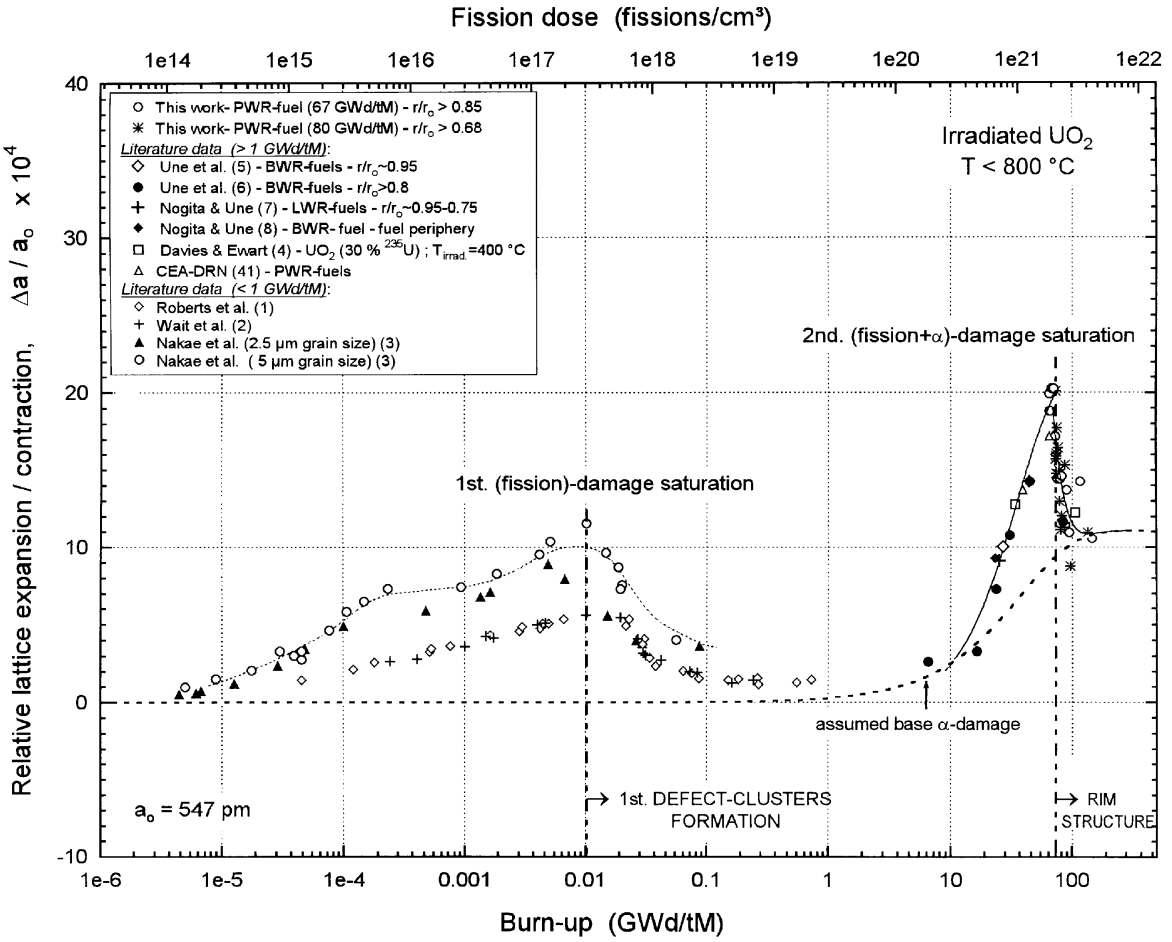

Fig. 9. Lattice expansion and contraction of irradiated fuels relative to unirradiated UO_2 without subtraction of α-damage, in logarithmic burn-up scale from the beginning of life to exposures beyond the rim-structure formation. Data of PWR and BWR-fuels (>1 GWd/tM): after several years of storage.

module. For UO_2, the Burgers vector is parallel to the [1 1 0]-direction [8,17,18], being its module: $b = (a/2)2^{1/2}$, where a is the lattice parameter.

Previous controversies [52,53] about the validity of the Keating and Goland statement [13,14] have been settled with the work of Willis et al. [54], showing that the condition for loops to influence the lattice dimension is that they must be small compared to the crystal size (approach of finite defects). At the other extreme, when the loop-size becomes comparable to the grain (or subgrain) size, the loops act as an extra plane of atoms, and do not modify the interplanar distances [54].

To assess both the volumetric density (N_L) and the size (R_0) of dislocation loops by X-ray diffraction analysis, a complementary equation to (2) is needed. For this, usually the influence of the loops on the Bragg-peak intensity is applied. According to Krivoglaz [16], the decrease of the diffracted intensity due to the effect of dislocation loops is expressed as

$$I_{hkl} = I_{0-hkl}e^{-2M} \quad \text{where } M = N_L R_0^3 (Qb)^{3/2} A(m) \tag{3}$$

with Q = scattering vector $= 4\pi \sin\theta/\lambda = 2\pi/d_{hkl}$, where b is the Burgers vector module and $A(m)$ is an orientation dependent constant with values ranging between 0.5 [16] and 1 [15].

The combination of Eqs. (2) and (3) at the condition of maximum lattice expansion at 70 GWd/tM ($\Delta a/a_{0-\max} = 1.1 \times 10^{-3}$, Fig. 8), for the intensity decrease of the (1 1 1)-peak shown in Fig. 3 (i.e., $2M \simeq -\ln(68/640) \simeq 2.24$ and $(Q{\cdot}b)^{3/2} = 21.35$) and for $A(m)$ values in the range 0.5–1, yielded loops radii and densities in the ranges $R_0 \simeq 19$–38 nm and $N_L \simeq 1.9$–7.6×10^{21} loops/m^3 (the lower the R_0, the higher the corresponding N_L). Not far from these values, dislocation loops in the size range 12–50 nm, with a density of 5.5×10^{20} loops/m^3, have been found experimentally in the central zone of a fuel with 74 GWd/tM

average burn-up [18]. On approaching the rim zone, higher loop densities than this last in the fuel centre are expected, i.e., becoming closer to the here determined values.

The above estimations must be considered, however, as approximations. First, the Bragg-peak intensity measurements are influenced by the statistics of diffracting planes which becomes poorer as the beam size decreases (our situation with the micro-beam). Second, it must be regarded that Eq. (2) implies in reality a summation over the whole loop sizes and densities, that only for simplicity is replaced by the product of the average values. A correct treatment would therefore require the consideration of the real loop size-density distributions. Despite this, the variation of Eq. (2) as a function of burn-up is thought to properly describe the lattice parameter evolution shown in Fig. 8.

Thus, it is suggested that during the lattice expansion step up to 70 GWd/tM (Fig. 8), a continuous growth of dislocation loops, both in size and density, would occur, until a critical loop size is achieved. Above this critical size, the loops may become too large to influence the lattice dimension and the lattice parameter would start to decrease. According to the conditions given in [54], this would occur when the loops reach the size of the original grains, or mediating grain subdivision, when they approach the size of the subgrains formed. Related to the rim formation process, this would correspond to the point (burn-up) at which a stable dislocation cell structure is formed [8,12], since, in principle, dislocation loops would grow only until they intersect the walls of the global dislocation network [55].

From different TEM observations, sizes of these preliminary formed subgrain domains in the rim-zone would range from few nanometers [56] to 40–200 nm [8,18]. Evolution from this configuration of cells and/or low-angle subgrain boundaries (polygonization case) [18] to randomly oriented, high-angle new grains (recrystallization case) would take place progressively at higher burn-ups during lattice expansion recovery. A proof of this would be electron backscattering patterns (EBSP) of irradiated fuels, indicating a transition from slightly mismatched subgrains in a strained matrix to randomly oriented subgrains in a less strained material, when moving the beam from the region adjacent to the rim zone to the pellet edge [57].

4.5. Comparison with rim models considering dislocation loops

The evolution of dislocation loops in high burn-up fuels has been treated recently in a theoretical model by Rest and Hofman [12]. There, a continued growth of loops with burn-up is considered via interaction with forest dislocations, until saturation occurs after a stable dislocation cell structure has formed. At saturation, occurring in the treated situation at >60 GWd/tM, the calculated loop size and density were $R_0 \cong 250$ nm and $N_L \cong 4 \times 10^{20}$ loops/m^3 [12], i.e., partly different to the values derived in the above section. Nevertheless, the derived dislocation-line density at saturation, calculated as $2\pi R_0 N_L \simeq 3 \times 10^{14}$ m/m^3 [12], is comparable to the range of values derived in the present work in Section 4.4 ($4.5–9 \times 10^{14}$ m/m^3).

As suggested in [55], it is explicitly shown in [12] that the growth of the dislocation loops in UO_2 under irradiation is limited by the size of the cells of the dislocation network. Under the conditions selected in [12], the stable cell size, coinciding with the maximum achievable loop size, was $\simeq$300 nm. However, the consideration of a real cell size distribution instead of a single average value would allow reproducing smaller saturated loop sizes [58], i.e., more congruent with the results in the above section. Also, tuning in [12] of the dislocation bias factor, i.e., the parameter that quantifies the preferential absorption of interstitials by dislocations [12,55], would allow reasonable fitting of the values in our Fig. 8 [58]. Thus, though differences in the preliminary derived numbers, the treatments in [12] and in the above section appear consistent.

4.6. Correlation with the matrix Xe-depletion and the porosity increase

Apart from the described correlation with the lattice defects evolution, the transition at 70 GWd/tM (Fig. 8) appears to be related to the displacement of Xe-atoms in the matrix and to the pore formation. Attention is recalled to Ref. [23], where the matrix Xe-depletion measured by EMPA is described. By comparison of our Fig. 8 with Fig. 2 of Ref. [23], it becomes evident that above $\simeq$70 GWd/tM the measured lattice contraction and matrix Xe-depletion follow equivalent decay laws in terms of local burn-ups. In addition to that, Fig. 5 indicates that the lattice contraction above 70 GWd/tM is concomitant with the porosity increase inside the rim-zone.

The connection between the above parameters is included partially in the volume balance equation for the defect-rich fuel. In general, the concentration of excess defects in the solid is given by the difference between the bulk and the lattice volume variations after a defect accumulation step [19]. If this difference is positive the predominant excess defects are vacancies and if it is negative the excess defects are mainly interstitials [16]. According to Nakae et al. [47], the general volume balance equation for the fuel may be then written as

$$[(\Delta V/V)(1-p)/(1-p_0) - (p-p_0)/(1-p_0)] - 3\Delta a/aC_v' = 0, \quad (4)$$

where $\Delta V/V$ is the bulk volume change (dilatometry or immersion density measurements), $3\Delta a/a$ the lattice

volume change, p_0 and p are the initial and burn-up dependent porosities and C'_v is the excess vacancies concentration. In Ref. [47] the quantity C'_v was interpreted as the difference between the total concentrations of vacancies and interstitials (from both Frenkel and Schottky defects), or as concentration of vacancies from only Schottky defects, whose ad-atoms in boundaries produce a net bulk volume increase.

The evolution of the parameter C'_v according to Eq. (4) was represented in Fig. 10 as a function of burn-up, for the two fuels described in the present work. Since we are here concerned with bulk volume changes caused by the fission gas atoms, the $\Delta V/V$ values in (4) were considered as given by the gas matrix swelling. For this bulk volume change, an approximate rate of $\Delta V/V(g) \widehat{=}$ 0.7%/10 GWd/tM was regarded as the difference between the total and the solid swelling rate, respectively, $\simeq$1%/10 GWd/tM [59] and 0.32%/10 GWd/tM [37]. The lattice parameter changes ($\Delta a/a$) were taken from Fig. 8 and the porosity values (p) from Fig. 5. The initial porosity (p_0) was fixed approximately at 4%.

As shown in Fig. 10, the introduction of the experimental values in Eq. (4) suggests a decrease of the excess vacancies concentration in the fuel, at the time that the local porosity increases steeply above $\simeq$70 GWd/tM (Fig. 5). Eq. (4) indicates also that under the condition of total excess vacancies exhaustion ($C'_v = 0$), suggested in Fig. 10 to occur above $\simeq$100 GWd/tM, the maximum achievable porosity in the fuel is roughly fixed by the accumulated bulk volume increase, i.e., the here assumed total gas matrix swelling. The small involved lattice volume changes ($\leqslant$0.3%, Fig. 8) imply only a slight modification of these figures. Under these conditions, for a local burn-up of e.g., $\simeq$180 GWd/tM at the pellet edge, only a maximum porosity of 15–17% would be achievable, starting from an initial porosity (p_0) of 3–5%. Furthermore, negative values of the quantity C'_v would indicate an overestimation of the measured local porosity, as it appears to be the case of the points marked with open symbols in Fig. 10.

Since Xe-atoms in matrix traps are assumed to be bound to excess vacancy clusters [60,61], e.g., in the

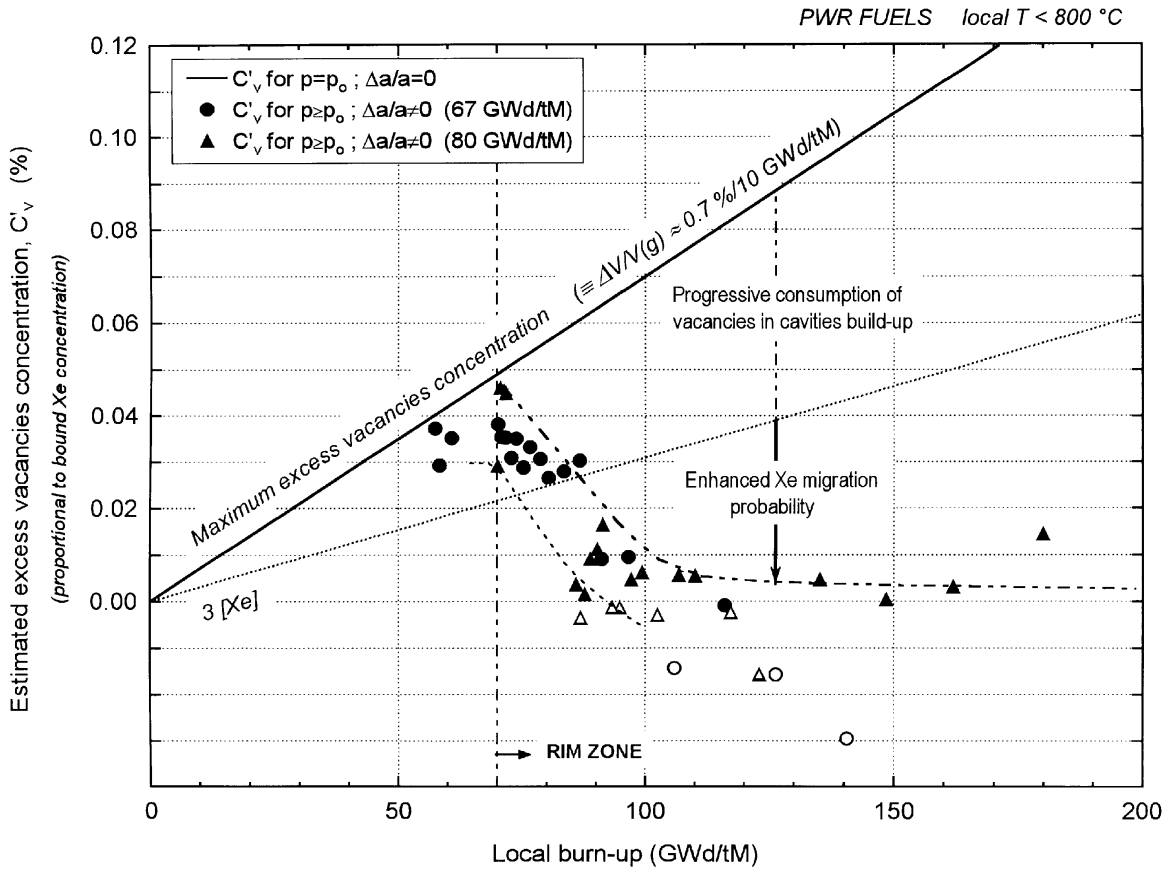

Fig. 10. Estimated excess vacancies concentration as a function of burn-up for the two fuels examined, according to Eq. (4). $C'_v = [\Delta V/V(g)(1-p)/(1-p_0) - (p-p_0)/(1-p_0)] - 3\Delta a/a$; $\Delta V/V(g)$ = matrix gas swelling $\approx$0.7%/10 GWd/tM; 3 [Xe] = vacancies demand to trap all Xe in trivacancies defects. Open symbols: out of range values ($C'_v < 0$) suggesting porosity overestimation.

so-called Schottky-trios (tri-vacancies consisting of one U- and two O-vacancies) [61], the quantity C'_v would indicate also the amount of potentially retained Xe-atoms. The curve 3 [Xe] vs burn-up plotted in Fig. 10 denotes the minimum amount of excess vacancies required to trap all the Xe atoms in tri-vacancies clusters. The created Xe atom concentration was calculated as [Xe] = Dose (fissions/cm^3) Xe_{yield}/N, being that Dose (fissions/cm^3) $\approx$BU(GWd/tM)$\times 2.8 \times 10^{19}$ [2], $Xe_{yield} = 0.27$ [37], N = total atoms per unit volume $\approx 12/a^3$ [47] and a = lattice parameter $= 5.47 \times 10^{-8}$ cm (Fig. 7). As seen in Fig. 10, up to $\simeq$70 GWd/tM it holds that $C'_v > 3$ [Xe], showing that at least from the number of available traps, a total retention of Xe in the fuel matrix is possible. On the other hand, the rather rapid decrease of C'_v between 70 and 100 GWd/tM (Fig. 10), as a result of the apparent consumption of vacancies in the creation of new cavities (coarsened bubbles, pores), implies also a strong decrease of the probability to retain Xe in matrix traps. This would agree with the findings, e.g., in [23] of an enhanced Xe depletion in this burn-up range.

The enhanced Xe-mobility above 70 GWd/tM does not necessarily imply an immediate release of this gas towards the open fuel volume. Contrarily, it seems that once enabled, the Xe-migration would be restricted to a very short spatial range around the pores, remaining the gas trapped in the porosity. Support of this would be the evidences that, even at high average burn-ups ($\simeq$80 GWd/tM), a high percentage of the produced fission gases ($\simeq$80%) remain trapped in the fuel [62].

In previous work it was stated that the formation of pores appeared as a key phenomenon in the rim process [22]. Evidences were provided that in its preliminary form the grain subdivision appears localised around pores [22,63] and that Xe-depletion is concomitant with the porosity growth even in absence of complete grain subdivision [63]. Congruently, theoretical works by other authors have shown that, assuming grain subdivision to be the vehicle facilitating the growth and gas feeding of rim pores, most probably this process would start localised around certain precursor cavities [12]. Thus, the hypothesis is here emphasized that the rim pores, e.g., formed like proposed in [12], would largely develop as closed Xe-reservoirs. Only the appearance of some pore interconnection, eventually at very high burn-ups (e.g. >180 GWd/tM local), would allow the release of gases to the exterior. Studies of the evolution of the pore connectivity as a function of burn-up appear therefore worthy.

4.7. Accumulated damage vs matrix gas concentration. Strain recovery implications

It has been shown in former sections that although small in comparison to the high doses involved a definite lattice distortion is accumulated during fission in the region adjacent to the rim-zone (onset), which is completely released during the rim-structure formation (Figs. 4,5,8,9).

However, as discussed in Section 4.3, probably not all the distortions caused during irradiation would be manifested in a shift of the Bragg-peak positions. This appears to be particularly the case of the Xe atoms in the matrix. Indeed, high-dose Xe implantation studies in UO_2 single-crystals have shown that beside the displacement of the Bragg reflections, the implanted Xe caused a widening of the diffraction peaks tails (Ω-scans), attributed to the formation of mosaic crystallites in the main crystal (polygonization) [64]. Interestingly, this effect was not present when rapidly outdiffusing species (Cs) were implanted. Hence, it was concluded that damage accumulation alone is not sufficient but also a high enough concentration of the impurity gas (Xe) is needed to cause the structure changes typical of the rim zone [64]. This may be also the reason why in the low-dose fission damage of UO_2, an equivalent rim structure formation did not occur although similar lattice dimension changes were induced as in the high burn-up case (α-damage suppressed) [3,47–50] (Figs. 8 and 9). The obvious feature lacking in the first case was a sufficient amount of matrix trapped Xe, on the contrary a very abundant species at high burn-ups.

Thus, it might be concluded that both a sufficient lattice damage (i.e., high enough number of point defects, forest and loop dislocations, etc.) and a sufficient concentration of fission gases in matrix traps, causing additional local straining, might accumulate in order to trigger the rim transformation. During the transformation, elimination of both effects would cause considerable strain release in the material, which may have a beneficial impact on various defect-sensitive properties of the fuel, e.g., eventually on the thermal conductivity. However, a potential improvement of this property after rim transformation may depend on the relative importance of the so-called 'damage' term, compared to the (worsening) effect of porosity and solid fission products [65]; both these last strongly increase in the rim zone.

5. Summary and conclusions

The various aspects treated in this paper can be resumed as follows:

- The lattice parameter of the fuel after discharge shows an important component of α-damage, which is assumed to reach its maximum at the pellet edge where the highest amount of α-emitting elements is present.
- Above this assumed saturating α-damage, a definite lattice damage accumulation is observed in the region near the onset of the rim-zone in high burn-up fuel. This damage decreases towards both the hotter centre and the cold periphery. The decrease towards

the pellet centre is attributed to thermal healing while the decrease towards the pellet edge is assigned to the formation of the rim structure.

- The damage release towards the pellet edge is coincident in radial position with the evolution of other properties within the rim-zone, e.g., depletion of matrix Xe atoms, increase of porosity and decrease of hardness. Moreover, in terms of local burn-ups, its rate seems basically to coincide with that of the matrix Xe depletion measured by EPMA. Since this contraction rate is much higher than that produced by dissolved foreign atoms in the lattice, solution effects are a priori excluded from the transformation.
- The observed lattice expansion–contraction behaviour can be explained alternatively by a saturation of primary interstitials with subsequent recombination with excess vacancies, or by a number saturation and enlargement of interstitial dislocation loops. The possible explanation via dislocation loops could have a back-up in a rim structure model, assuming growth of these loops with the increase of burn-up, until saturation is reached when a stable dislocation cell structure is formed.
- Apart from the described lattice distortion healing, the development of the rim zone is apparently associated with the transfer of substantial amounts of Xe-atoms from matrix traps to pores, what would contribute to additional local strain release. It is suggested that both effects would imply a local improvement of the damage-sensitive properties of the fuel, e.g., the thermal conductivity. However, the potential improvement of this last property could be masked by the worsening effect of the porosity and the fission products concentration, both increasing in the rim zone.

As a conclusion, it must be added that the formation of the rim structure requires considerable accumulations of both lattice damage and fission gas atoms in matrix traps. The lattice damage alone is not sufficient to trigger the process. Both subgrain formation and pore growth start after achievement of the critical conditions (critical burn-up). Although the explicit linkage between these two partial processes was not clear in the present data, it is important to remark that both processes converge cooperatively in localised points of the fuel matrix, generating closed pores that would re-trap the gas of the surroundings. These new traps would retard the migration of gases (particularly Xe) to the free surface, probably helping so to maintain the gas release of the rim zone within acceptable limits.

Acknowledgements

The authors are indebted to Daniel Baron, EdF, Les Renardières, France, for detailed local burn-up calculations with the CEA-code APPOLO-2, and to R. Manzel of Siemens-KWU for providing the high-burn-up fuel-samples. Also, permission of C. Prunnier, CEA-Direction of Nuclear Reactors (DRN) for the citation of the unpublished results of CEA on annealed-aged fuels is gratefully recognised. Revision of the manuscript by J. Rest (ANL) and comments by Hj. Matzke and C.T. Walker (ITU) and P. Dehaudt (CEA-Grenoble) are gratefully acknowledged.

References

[1] L.E. Roberts, P. Brook, J.R. Findlay, B.R. Frost, L.E. Russell, J.B. Sayers, E.Wait, in: Proceedings of the Third UNInternational Conference on Peaceful Uses of Atomic Energy, P/155, vol. 11, Geneva, 1964, p. 464.
[2] E. Wait, M.J. Duck, A.C. Fox, E.E. Jackson, A.R. Junkinson, Radiation damage in solids, IAEA 2 (1962) 231.
[3] N. Nakae, A. Harada, T. Kirihara, S. Nasu, J. Nucl. Mater. 71 (1978) 314.
[4] J.H. Davies, F.T. Ewart, J. Nucl. Mater. 41 (1971) 143.
[5] K. Une, Y. Tominaga, S. Kashibe, J. Nucl. Sci. Technol. 28 (1991) 409.
[6] K. Une, K. Nogita, S. Kashibe, M. Imamura, J. Nucl. Mater. 188 (1992) 65.
[7] K. Nogita, K. Une, J. Nucl. Sci. Technol. 30 (1993) 900.
[8] K. Nogita, K. Une, Nucl. Instrum. and Meth. B 91 (1994) 301.
[9] K. Nogita, K. Une, J. Nucl. Sci. Technol. 31 (1994) 929.
[10] I.L.F. Ray, H. Thiele, Hj. Matzke, J. Nucl. Mater. 188 (1992) 90.
[11] J. Rest, G.L. Hofman, J. Nucl. Mater. 210 (1994) 187.
[12] J. Rest, G.L. Hofman, J. Nucl. Mater. 277 (2000) 231.
[13] D.T. Keating, A.N. Goland, J. Appl. Phys. 39 (1968) 6018.
[14] A.N. Goland, D.T. Keating, J. Appl. Phys. 41 (1970) 814.
[15] L.D. Penteleyev, V.T. Deripasko, Phys. Met. Metalloved. 50 (1980) 129.
[16] M.A. Krivoglaz, X-Ray and Neutron Diffraction in Nonideal Crystals, Springer, Berlin, 1995, Chapters 3&4.
[17] A.D. Whapham, B.E. Sheldon, Philos. Mag. 12 (1965) 1179.
[18] I.L.F. Ray, Hj. Matzke, H.A. Thiele, M. Kinoshita, J. Nucl. Mater. 245 (1997) 115.
[19] W.J. Weber, J. Nucl. Mater. 98 (1981) 206.
[20] W.J. Weber, Radiat. Eff. 83 (1984) 145.
[21] Hj. Matzke, Radiat. Eff. 64 (1982) 3.
[22] J. Spino, K. Vennix, M. Coquerelle, J. Nucl. Mater. 231 (1996) 179.
[23] C. Walker, J. Nucl. Mater. 275 (1999) 56.
[24] D. Papaioannou, J. Spino, Rev. Sci. Instrum., to be published.
[25] R. Manzel, M. Coquerelle, in: ANS International Topical Meeting on Light Water Reactor Fuel Performance, 2–6 March, Portland, OR, USA, 1997, pp. 463–470.
[26] Seifert XDALK 3000 Software, Revision 1.4, Rich.Seifert & Co.GmbH Röntgenwerk, Ahrensburg, Germany, 1993.
[27] H.W. King, E.A. Payzant, in: J.V. Gilfrich (Ed.), Advances in X-Ray Analysis, vol. 36, Plenum, New York, 1993, pp. 663–670.

[28] Silicon standard for X-Ray Powder Diffractometry. National Institute for Standards and Technology, Gaithersburg, MD 20899, USA.
[29] JCPDS-Powder Diffraction Data Files, PDF-2, International Centre for Diffraction Data, Newton Square, PA 19073-3273, USA, 1996.
[30] J. Cobos, D. Papaioannou, J. Spino, M. Coquerelle, J. Alloys Compounds 271–273 (1998) 610.
[31] K. Une, M. Oguma, J. Nucl. Sci. Technol. 20 (1983) 844.
[32] S. Ishimoto, M. Irai, K. Ito, Y. Korei, J. Nucl. Sci. Technol. 31 (1994) 796.
[33] P.G. Lucuta, B.J. Palmer, Hj. Matzke, D.S. Hartwig, Report AECL-10117, 1989.
[34] P.G. Lucuta, R.A. Verall, Hj. Matzke, I.J. Hastings, in: International Conference on CANDU fuel 3, 4–8 October, Chalk River, Canada, 1992, pp. 2–61.
[35] A.G. Croff, Origen-2, A revised and up-dated version of the OAK Ridge Isotope Generation and Depletion Code, Report ORNL-5621, 1980.
[36] APOLLO-2 Code, CEA, CEN-Saclay, France.
[37] D.R. Olander, Fundamental Aspects of Nuclear Reactor Fuel Elements, Energy Research and Development Administration, TID-26711-P1, 1976.
[38] H. Kleykamp, J. Nucl. Mater. 131 (1985) 221.
[39] H. Kleykamp, J. Nucl. Mater. 171 (1990) 181.
[40] Hj. Matzke, J. Nucl. Mater. 223 (1995) 1.
[41] B. Clavier, Y. Gourel, Measures du paramètre cristallins des crayons Gravelines et Saint-Laurent B1 par diffraction des rayons X. CEA, Direction of Nuclear Reactors (DRN), Report DMT-94/07/SETIC/LECR-94/01-1994.
[42] T. Muromura, T. Adachi, H. Takaeishi, Z. Yoshida, T. Yamamoto, K. Ueno, J. Nucl. Mater. 206 (1993) 82.
[43] H. Kleykamp, J. Nucl. Mater. 206 (1993) 82.
[44] H. Kleykamp, J.O.A. Paschoal, R. Pejsa, F. Thümmler, J. Nucl. Mater. 130 (1985) 426.
[45] J.O.A. Paschoal, H. Kleykamp, F. Thümmler, J. Nucl. Mater. 151 (1987) 10.
[46] H. Kleykamp, R. Pejsa, J. Nucl. Mater. 124 (1984) 56.
[47] N. Nakae, T. Kirihara, S. Nasu, J. Nucl. Mater. 74 (1978) 1.
[48] T. Kirihara, N. Nakae, H. Matsui, M. Tamaki, in: H. Blank, R. Lindner (Eds.), Plutonium and other Actinides, North-Holland, Amsterdam, 1976, p. 903.
[49] H. Matsui, M. Horiki, M. Tamaki, T. Kirihara, in: F.A. Garner, C.H. Henager Jr., N. Iagata (Eds.), Influence of Radiation on Material Properties 13th International Symposium (Part II), ASTM STP 956, American Society for Testing Materials, Philadelphia, 1987, p. 593.
[50] M. Akabori, K. Shiba, J. Nucl. Mater. 101 (1981) 184.
[51] Hj. Matzke, Radiat. Eff. 64 (1982) 3.
[52] P.M. Kelly, J. Appl. Phys. 44 (1973) 3782.
[53] C.J. Howard, T. Sabine, J. Phys. C 7 (1974) 3453.
[54] J.R. Willis, R. Bullough, A.M. Stoneham, Philos. Mag. A 1 (1983) 95.
[55] P.T. Heald, M.V. Speight, Acta Met. 23 (1975) 1389.
[56] K. Nogita, K. Une, J. Nucl. Mater. 250 (1997) 244.
[57] S. Bengtsson, IAEA-Technical Committee Meeting on Advances in Pellet Technology for Improved Performance at High Burn-up, 28 October–1 November 1996, Tokyo, Japan, Paper 3/6.
[58] J. Rest, Argonne National Laboratory, USA, private communication, February 2000.
[59] H. Assmann, R. Manzel, J. Nucl. Mater. 68 (1977) 360.
[60] J.R. MacEwan, W.H. Stevens, J. Nucl. Mater. 11 (1964) 1.
[61] Hj. Matzke, Radiat. Eff. 53 (1980) 219.
[62] R. Manzel, C.T. Walker, in: KTG Meeting on Verification of Fuel Performance through Hot Cell Examinations and Experiments, Karlsruhe, Germany, 2–9 February/1 March 2000.
[63] J. Spino, D. Baron, M. Coquerelle, A.D. Stalios, J. Nucl. Mater. 256 (1998) 189.
[64] Hj. Matzke, A. Turos, G. Linker, Nucl. Instrum. and Meth. B 91 (1994) 294.
[65] P.G. Lucuta, Hj. Matzke, I.J. Hastings, P.G. Klemens, in: K.E. Wilkes, R.B. Dinwiddie, R.S. Graves (Eds.), Thermal Conductivity, vol. 23, Technomic Publishing Company, Lancaster-Basel, 1996.